

Prediction of rotating losses in heteropolar radial magnetic bearings

David C. Meeker

Eric H. Maslen

Published *Journal of Tribology*, 120(3):629-635, July 1998

Abstract: Previously, thin plate assumptions have been used to obtain a one-dimensional eddy current model for predicting the stationary, transformer-type losses in magnetic bearings built out of laminated material. Using similar assumptions as in the 1-D eddy current model, rotating losses can be predicted for a laminated heteropolar radial magnetic bearing. The thin plate model of rotating losses yields a hybrid analytical-boundary element model that is computationally inexpensive to implement. Predictions from this model compare favorably to losses experimentally measured in rotor run-down tests.

1 Introduction

Classically, eddy currents in laminated transformer cores have been treated with the model presented by Stoll [1]. To simplify the eddy current problem, this model idealizes the eddy current problem as “locally one-dimensional because the penetration distance is small compared to the other [lamination] dimensions.” With this assumption, the eddy current problem is reduced to a one-dimensional diffusion equation that can be solved analytically.

The 1-D eddy current model has been applied with success to transformer cores [2] [3] [4], magnetic bearings [5] [6] and magnetic shielding [7]. In all of these cases, however, eddy currents are induced by variation of the applied magnetic field in time, rather than by motion.

Because of the simplicity of the 1-D model, it is tempting to try a similar approach to modeling eddy currents generated by motion in laminated magnetic bearing rotors. It has been suggested that the classical eddy current loss equations derived for stationary transformers might be applied directly to rotating losses with an “effective frequency” and “effective volume” based on rotor dimensions and speed [8] [9]. However, the choice of effective frequency and volume is somewhat heuristic.

The goal of the present work is to model the rotational eddy current losses in heteropolar radial magnetic bearings in a consistent fashion that does not require the choice of an effective frequency and volume. To simplify the formulation, the laminated structure of the journal is exploited. Using a thin plate approach similar to the 1-D model applied to transformer-type losses, a simplified model is derived that gives an analytical solution for flux density inside the journal in terms of the magnetic scalar potential at the journal surface.

By combining the analytical model inside the rotor with a boundary element model of the magnetic field in

the air between the pole tips and the rotor surface, the scalar potential at the rotor surface can be determined, and therefore the field inside the rotor, for any configuration of coil currents. The rotating losses are then found by summing the loss associated with each Fourier component of the field at the rotor surface, similar to the qualitative approach in [10]. The validity of this model is assessed by comparing the predicted power losses to losses derived from experimental run-down tests. Predicted losses show a good agreement to experimentally derived losses.

2 Model development

In this work, it is assumed that the rotor is composed of a linear material obeying the steady-state Maxwell's equations:

$$\nabla \times H = J \quad (1)$$

$$\nabla \cdot B = 0 \quad (2)$$

$$\nabla \times E = \nabla \times V \times B \quad (3)$$

$$\nabla \cdot J = 0 \quad (4)$$

and the linear constitutive laws:

$$B = \mu H \quad (5)$$

$$J = \sigma E \quad (6)$$

From the analysis of transformer-type losses including hysteresis in [1], electrical losses including hysteresis are only be slightly higher than losses without hysteresis at high excitation frequencies. It is reasonable to expect that the same is true at high rotor speeds. For simplicity, hysteresis effects are neglected in the present analysis.

The typical eight-legged heteropolar radial bearing is pictured in Figure 1. To simplify the analysis, it will be assumed that the journal can be “unrolled” into a periodic sheet, as pictured in Figure 2. In the unrolled model, every point in the journal has the velocity

$$V \equiv r_o \omega \mathbf{a}_2 \quad (7)$$

where r_o is the outer radius of the journal, ω is the rotational speed in rad/s, and \mathbf{a}_2 is a unit vector associated with the θ coordinate. Eq. (3), the mechanism through which motion-induced eddy currents are created, can then be simplified using the definition of velocity from (7):

$$\nabla \times E = -\omega \frac{\partial B}{\partial \theta} \quad (8)$$

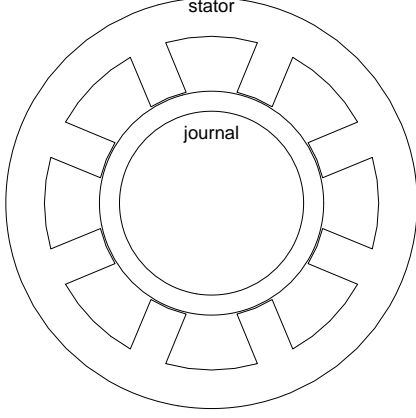


Figure 1: Typical eight legged heteropolar bearing.

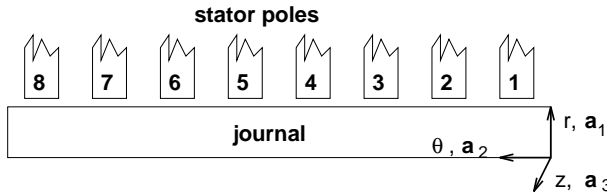


Figure 2: “Unrolled” heteropolar bearing.

A partial differential equation describing the flux distribution inside one lamination is derived by first taking the curl of (1):

$$\nabla \times \nabla \times H = \nabla \times J \quad (9)$$

Then, the constitutive laws are used to write (9) in terms of B and E :

$$\nabla \times \nabla \times B = \sigma \mu_o \nabla \times E \quad (10)$$

Applying equation (2) to (10) to enforce the zero divergence of B yields:

$$-\nabla^2 B = \sigma \mu_o \nabla \times E \quad (11)$$

Finally, (8) is substituted into (11) to give the differential equation describing the flux density inside each lamination:

$$\nabla^2 B = \omega \sigma \mu \frac{\partial B}{\partial \theta} \quad (12)$$

No thin-plate assumption has yet been made. In the unrolled domain,

$$\nabla^2 \equiv \frac{\partial^2}{\partial r^2} + \frac{1}{r_o^2} \frac{\partial^2}{\partial \theta^2} + \frac{\partial^2}{\partial z^2} \quad (13)$$

If the rotor is composed of thin laminations in the \mathbf{a}_3 direction, the cross-lamination second-order term $\frac{\partial^2}{\partial z^2}$ can be expected to dominate $\nabla_{r,\theta}^2 B$ because the second derivatives of B with respect to z must be huge to affect any change B across the lamination thickness. The thin-plate model assumes that the r and θ second-order

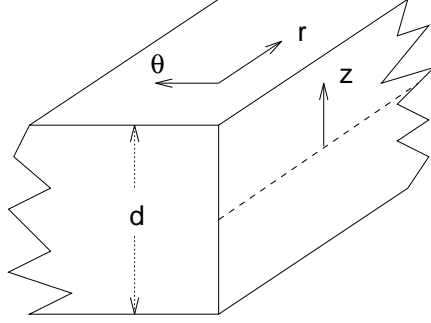


Figure 3: Detailed view of a single rotor lamination.

components are so insignificant compared to the z component that they can be neglected altogether. Applying the thin-plate assumption to (12) yields a simplified eddy current model driven by journal motion:

$$\frac{\partial^2 B}{\partial z^2} = \omega \sigma \mu \frac{\partial B}{\partial \theta} \quad (14)$$

Equation (14) is very similar to Stoll’s 1-D diffusion equation; the difference is that for transformer-type losses, the first-order derivative on the right-hand side is with respect to time rather than the spatial coordinate θ .

Since the unrolled domain is 2π periodic in the θ coordinate, the solution for B is expected to consist of harmonics in θ . A phasor representation [11] can be adopted where B is understood to be the real part of

$$\sum_{n=0}^{\infty} b_n e^{jn\theta} \equiv \sum_{n=0}^{\infty} b_n (\cos n\theta + j \sin n\theta) \quad (15)$$

where b_n is a complex number denoting the magnitude and phase of the n^{th} harmonic component of B . Since the system is linear, each harmonic can be considered separately and the results for all harmonics superimposed to yield a solution for B .

Substituting the phasor representation for B into (14) yields

$$\frac{\partial^2 b_n}{\partial z^2} e^{jn\theta} = jn\omega \sigma \mu b_n e^{jn\theta} \quad (16)$$

Each side can be divided by $e^{jn\theta}$:

$$\frac{\partial^2 b_n}{\partial z^2} = jn\omega \sigma \mu b_n \quad (17)$$

In the phasor representation, the flux distribution for each harmonic is merely an ordinary differential equation respect to z , the coordinate in the plate thickness direction.

Boundary conditions must be specified if (17) is to be solved for the flux distribution in the laminated rotor. Let each lamination be of thickness d , and let the $z = 0$ at the center of the lamination of interest, as illustrated in Figure 3. Since the model is pseudo-2-dimensional (that is, the flux density distribution is the same in every lamination in the journal), one would expect no \mathbf{a}_3

component of b_n at the interface between laminations. The axial component of B , $b_n \cdot \mathbf{a}_3$, is therefore equal to zero everywhere. The \mathbf{a}_1 and \mathbf{a}_2 boundary condition at interface between laminations then specified as

$$B[r, \theta, \frac{d}{2}] = B_o[r, \theta]; \quad \frac{\partial B}{\partial z}[r, \theta, 0] = 0 \quad (18)$$

where $B_o[r, \theta]$ is some unknown function of r and θ that is yet to be determined. Converting the boundary conditions into the phasor representation gives:

$$b_n[r, d/2] = b_{n,o}[r]; \quad \frac{\partial b_n}{\partial z}[r, 0] = 0 \quad (19)$$

where $b_{n,o}$ represents the n^{th} harmonic component of B_o . Equation (17) subject to (19) is the same equation that must be solved in [1] for transformer-type losses; the solution is

$$b_n[r, z] = b_{n,o}[r] \frac{\cosh[\sqrt{jn\omega\sigma\mu}z]}{\cosh[\sqrt{jn\omega\sigma\mu}\frac{d}{2}]} \quad (20)$$

The average flux density, \bar{b}_n , at in the lamination is found by integrating across the lamination:

$$\begin{aligned} \bar{b}_n &= \frac{2}{d} \int_0^{d/2} b_n[r, z] dz \\ &= b_{n,o} \frac{\tanh[\sqrt{jn\omega\sigma\mu}\frac{d}{2}]}{\sqrt{jn\omega\sigma\mu}\frac{d}{2}} \end{aligned} \quad (21)$$

However, the boundary field distribution, $b_{n,o}$, has not yet been determined in the \mathbf{a}_1 and \mathbf{a}_2 directions. This boundary condition should be chosen such that zero divergence of B , equation (2), is satisfied. To solve for an appropriate B_o , define magnetic scalar potential Ω as

$$-\mu \nabla \Omega = B_o \quad (22)$$

Since there is no \mathbf{a}_3 component of B , zero divergence is satisfied if

$$\nabla_{r,\theta} \cdot B_o = 0 \quad (23)$$

The zero divergence of B_o written in terms of scalar potential is

$$\nabla^2 \Omega = 0 \quad (24)$$

Transforming (24) into the phasor representation yields:

$$\frac{\partial^2 \Omega_n}{\partial r^2} - \left(\frac{n}{r_o}\right)^2 \Omega_n = 0 \quad (25)$$

It is reasonable to impose the boundary condition

$$\frac{\partial \Omega_n}{\partial r} = 0; \quad r = r_i \quad (26)$$

which requires that no flux crosses the inner radius of the journal at $r = r_i$. At $r = r_o$, the outer radius of the journal, the value of Ω_n is some specified value, $\Omega_{n,o}$:

$$\Omega_n[r_o] = \Omega_{n,o} \quad (27)$$

Solving (25) with these boundary conditions gives the scalar potential for each harmonic in terms of scalar potential at the journal surface:

$$\Omega_n[r] = \Omega_{n,o} \frac{\cosh[\frac{n}{r_o}(r - r_i)]}{\cosh[\frac{n}{r_o}(r_o - r_i)]} \quad (28)$$

Eqs. (20) and (28) are combined to describe each harmonic of flux density in the journal:

$$\begin{aligned} b_n &= -\mu \Omega_{n,o} \left(\frac{n}{r_o}\right) \left(\frac{\cosh[\sqrt{jn\omega\sigma\mu}z]}{\cosh[\sqrt{jn\omega\sigma\mu}\frac{d}{2}]} \right) * \\ &\quad \left(\frac{\sinh[\frac{n}{r_o}(r - r_i)]}{\cosh[\frac{n}{r_o}(r_o - r_i)]} \mathbf{a}_1 + j \frac{\cosh[\frac{n}{r_o}(r - r_i)]}{\cosh[\frac{n}{r_o}(r_o - r_i)]} \mathbf{a}_2 \right) \end{aligned} \quad (29)$$

Through (29), the flux density is defined in terms of unknown Fourier series coefficients of the magnetic scalar potential at the rotor surface. If an input-output relationship between applied potential at the rotor surface to resulting flux passing normal to the rotor surface is formed, the analytical solution for the field inside the journal can be combined with a computational model of the rest of the bearing to determine the unknown distribution $\Omega_o[\theta]$ at the rotor surface.

To simplify the analysis, it will be assumed that the flux in the gap is purely 2-dimensional. However, the solution in the lamination is a function of z , as can be seen in (20). It will be assumed that a transition between the 2-d solution in the gap and the fully-developed profile described by (20) takes place in a very thin skin region near the surface of the rotor. The interface with the air is then modeled by a conservation of flux passing normal to the air-iron interface:

$$(\text{air}) (B \cdot \mathbf{a}_1) = (\text{iron}) (\bar{B} \cdot \mathbf{a}_1) \quad (30)$$

or for each harmonic:

$$(\text{air}) (b_n \cdot \mathbf{a}_1) = (\text{iron}) (\bar{b}_n \cdot \mathbf{a}_1) \quad (31)$$

In terms of scalar potential, the conservation condition is

$$\mu_o \frac{\partial}{\partial r} \left[(\text{air}) \Omega_n \right] = \left(\frac{\mu \tanh[\sqrt{jn\omega\sigma\mu}\frac{d}{2}]}{\sqrt{jn\omega\sigma\mu}\frac{d}{2}} \right) \frac{\partial}{\partial r} \left[(\text{iron}) \Omega_n \right] \quad (32)$$

For continuity of H on the air-iron boundary,

$$(\text{air}) \Omega_n = (\text{iron}) \Omega_n \quad (33)$$

By differentiating (28) with respect to r , and substituting into (32), a boundary condition results that relates the applied scalar potential on the journal surface, Ω_n , to its normal derivative on the air side of the iron-air interface:

$$\frac{\partial \Omega_n}{\partial r} = \mu_r \left(\frac{n}{r_o}\right) \left(\frac{\tanh[\sqrt{jn\omega\sigma\mu}\frac{d}{2}]}{\sqrt{jn\omega\sigma\mu}\frac{d}{2}} \right) \tanh[\frac{n}{r_o}(r_o - r_i)] \Omega_n \quad (34)$$

This expression can be re-arranged into real and imaginary parts as

$$\frac{\partial \Omega_n}{\partial r} = (G_r + jG_i)\Omega_n \quad (35)$$

where

$$G_r = \mu_r \left(\frac{n \delta_n}{r_o d} \right) \left(\frac{\sin \frac{d}{\delta_n} + \sinh \frac{d}{\delta_n}}{\cos \frac{d}{\delta_n} + \cosh \frac{d}{\delta_n}} \right) \tanh \left[\frac{n}{r_o} (r_o - r_i) \right] \quad (36)$$

$$G_i = \mu_r \left(\frac{n \delta_n}{r_o d} \right) \left(\frac{\sin \frac{d}{\delta_n} - \sinh \frac{d}{\delta_n}}{\cos \frac{d}{\delta_n} + \cosh \frac{d}{\delta_n}} \right) \tanh \left[\frac{n}{r_o} (r_o - r_i) \right] \quad (37)$$

and

$$\delta_n = \left(\frac{2}{n \omega \sigma \mu} \right)^{\frac{1}{2}} \quad (38)$$

is the skin depth associated with each harmonic. Eq. (34) specifies the relationship between potential in the air to the normal gradient of potential at the surface of the rotor. By solving for the potential distribution in the *in the air only* subject to boundary condition (34), the field inside the rotor is uniquely specified by (29).

3 Power loss

If the magnetic scalar potential is known at the rotor surface, the field distribution in the journal is known, and eddy current power losses can be computed. This loss, P , is found by integrating resistive power loss over the volume of the rotor:

$$P = \int_{r_i}^{r_o} \int_{-\frac{d}{2}}^{\frac{d}{2}} \int_0^{2\pi} \left(\frac{1}{\sigma} \right) J \cdot J r_o dz dr d\theta \quad (39)$$

Current density J is found via (1), by taking the curl of the field intensity. Since the r and θ variation of H are described by scalar potential Ω , $J \cdot J$ simplifies considerably to

$$J \cdot J = \left(\frac{\partial H_1}{\partial z} \right)^2 + \left(\frac{\partial H_2}{\partial z} \right)^2 \quad (40)$$

By orthogonality of sines and cosines, cross-products between different harmonics integrate to zero when (40) is evaluated over the entire volume of the journal. The power loss contributions from each harmonic can be considered separately and the results summed to get the total motion-induced power loss:

$$P = \sum_{n=0}^{\infty} P_n \quad (41)$$

For each harmonic, the power loss is

$$P_n = \frac{\pi r_o}{\sigma \mu} \int_{r_i}^{r_o} \int_{-\frac{d}{2}}^{\frac{d}{2}} \left| \frac{\partial b_n}{\partial z} \right|^2 dz dr \quad (42)$$

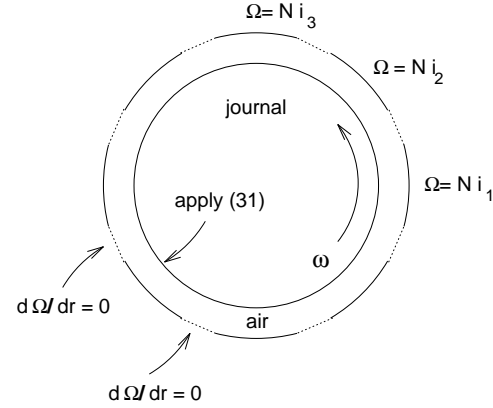


Figure 4: Simplified computational domain for modeling fringing effects.

where $\frac{\partial b_n}{\partial z}$ is found by differentiating (29) with respect to z . Integrating (42) yields:

$$P_n = |\Omega_{n,o}|^2 \left(\frac{2\pi n}{\sigma \delta_n} \right) \tanh \left[\frac{n}{r_o} (r_o - r_i) \right] \left(\frac{\sinh \frac{d}{\delta_n} - \sin \frac{d}{\delta_n}}{\cosh \frac{d}{\delta_n} + \cos \frac{d}{\delta_n}} \right) \quad (43)$$

Equation (43) is the loss for each lamination; this loss must be multiplied by the number of laminations in the journal to get the total bearing losses.

4 Incorporation of the journal solution with the bearing structure

If the field at the surface of the rotor is known, the rotating power loss can be determined via (43). As noted by Matsumura [10], the distribution of flux on the air-iron boundary has a large influence on the resulting power losses, and the motion-induced eddy currents somewhat alter the field distribution from the zero speed form. To determine the correct potential distribution at the surface of the rotor, the analytical solution inside the rotor must be coupled to a numerical solution for the field in the air between the poles and rotor surface.

An elaborate finite element or boundary element model could be used to represent the stator. For the purposes of this study, however, a very elaborate model is unnecessarily complicated. The goal is to model the fringing of flux around the edges of the poles correctly. To perform this task, it is sufficient to use the simple computational domain pictured in Figure 4. The computational domain is a thin annulus of air between the rotor surface and pole tips.

If the stator is built of highly permeable material, the stator back-iron can be considered magnetically “grounded” at zero potential. The potential on a section of the outside boundary of the annulus associated with the k^{th} pole can then be specified to be $N i_k$, the number of Amp-Turns of current flowing in the coil around the k^{th} pole.

Between pole tips, the boundary condition $\partial\Omega/\partial r = 0$ is applied. This boundary condition forces all flux to

pass the outer boundary of the annulus through the pole faces.

On the inside surface of the air annulus, boundary condition (34) is applied. Equation (34) is a phasor relationship between potential and its normal derivative on the boundary; to apply a numerical method, this boundary condition must be written in terms of spatial field values at points on the boundary of the computational domain. To apply the boundary condition, the spatial boundary values must be transformed into the phasor representation, the boundary conditions applied, and then transformed back into spatial coordinates. The transformation to phasor form is

$$\Omega_{n,o} = \frac{1}{\pi} \int_0^{2\pi} (\Omega_o[\theta] \cos n\theta - j \Omega_o[\theta] \sin n\theta) d\theta ; \quad n > 0 \quad (44)$$

$$\Omega_{0,o} = \frac{1}{2\pi} \int_0^{2\pi} \Omega_o[\theta] d\theta \quad (45)$$

However, the boundary is represented by a finite number of elements. Specifically, let the rotor surface be divided into m discrete elements. Inside each element, the scalar potential and normal gradient of scalar potential are approximated with constant trial functions. Equations (44) and (45) can then be approximated by the discrete transforms:

$$\Omega_{n,o} = \frac{2}{m} \sum_{k=1}^m (\Omega_o[k] \cos[nk \delta\theta] - j \Omega_o[k] \sin[nk \delta\theta]) \quad (46)$$

$$\Omega_{0,o} = \frac{1}{m} \sum_{k=1}^m \Omega_o[k] \quad (47)$$

where $\Omega_o[k]$ is the value of scalar potential at the center of the k^{th} element, and $\delta\theta$ is the length of each element in radians. Eqs. (46) and (47) are a linear transformation between the spatial and phasor representations of Ω on the rotor surface. Since there are only a finite number of boundary elements, only the first $\frac{m}{2}$ harmonics can be represented.

Since boundary condition (34) couples all boundary nodal values, it is unsuitable for use with a finite element scheme in which bandedness of the resulting stiffness matrix is essential to an efficient solution. Instead, a boundary element analysis is indicated. A boundary element scheme trades a large but banded matrix for a much smaller but full matrix. Applying a boundary condition that couples together all boundary nodes is consistent with the boundary element formulation. A detailed description of the boundary method with constant trial function elements applied to solving $\nabla^2\Omega = 0$ is contained in [12].

5 Comparison of model to experimentally measured losses

5.1 Identification of materials properties

It is apparent from the inspection of (43) that the rotating eddy current losses are strongly dependent on the

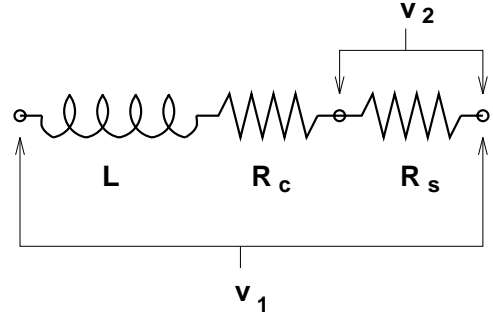


Figure 5: Ring test circuit.

magnetic permeability, μ , and the electrical conductivity, σ , of the journal material. These properties may vary widely for a particular material depending upon heat treatment. To get accurate materials properties to use for the rotating loss model, these properties must be accurately determined.

The desired materials properties can be obtained by testing the frequency response of a test ring built from the same batch of laminations from which the journal was constructed. To perform the test, the laminated test ring is wound with a number of turns of wire to form a simple choke. A sinusoidal excitation of different frequencies is applied across this winding. The time-varying nature of the excitation induces eddy currents in the test ring. From Stoll, the effect of these eddy currents can be thought of as modifying the permeability of the core material. Derived from a thin plate model, the frequency-dependent permeability of the core material is:

$$\mu_{fd}[j\hat{\omega}] = \mu \frac{e^{-\frac{\Theta}{2}} \tanh[e^{-\frac{\Theta}{2}} \sqrt{j\hat{\omega}\sigma\mu} \frac{d}{2}]}{\sqrt{j\hat{\omega}\sigma\mu} \frac{d}{2}} \quad (48)$$

where $\hat{\omega}$ is the frequency of excitation. In this expression, the effects of hysteresis in the core material is idealized as a pure phase lag between B and H of Θ radians. Including the effects of eddy currents and hysteresis, the frequency-dependent inductance of the coil is:

$$L[j\hat{\omega}] = \frac{N^2 a \mu_{fd}[j\hat{\omega}]}{\pi D} \quad (49)$$

where N is the number of turns wound around the core, a is the cross-sectional area, and D is the mean diameter of the ring. The frequency response of the ring is tested with the circuit pictured in Figure 5. The input is voltage v_1 is supplied across the coil and a sensing resistor, R_s . The output is the voltage v_2 across the sensing resistor, which is proportional to current in the coil. The overall transfer function of the test circuit is:

$$\frac{v_2}{v_1} = \frac{R_s}{j\hat{\omega}L[j\hat{\omega}] + R_c + R_s} \quad (50)$$

Eddy currents and hysteresis cause a substantial deviation in frequency response from what would be expected in the absence of eddy currents. By fitting the permeability, conductivity, and hysteresis angle so that (50)

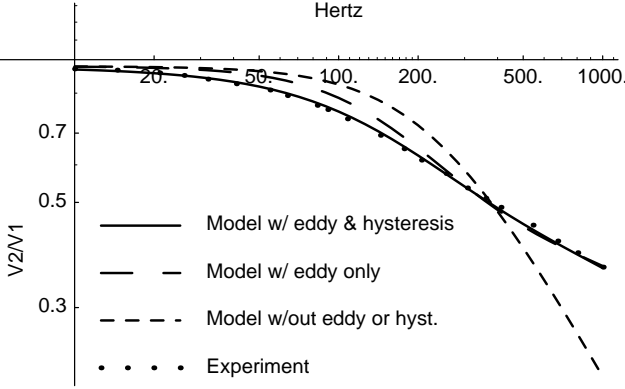


Figure 6: Magnitude response of ring test circuit.

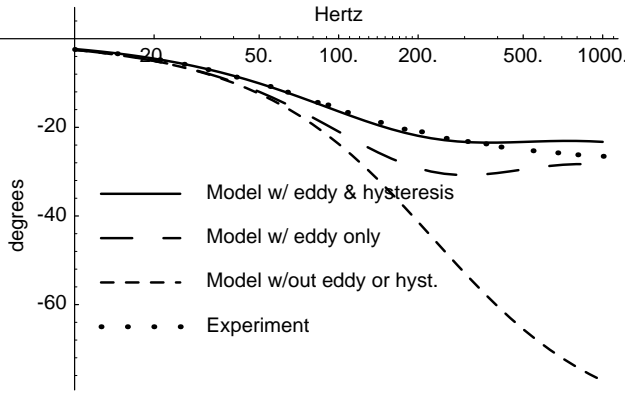


Figure 7: Phase shift ring test circuit.

closely matches the measured response of the circuit, the materials properties of the core material are identified.

This procedure was used to find the materials properties of the high-speed test rig described by Kasarda *et al* [8]. A test ring was constructed out of 14 mil, 3% silicon-iron laminations with an inner diameter of 2.54 cm, an outer diameter of 3.175 cm, and a length of 1.65 cm. The ring was tested at a number of frequencies between 10 and 1000 Hz. The coil and sense resistances were measured as $0.50\ \Omega$ and $15.30\ \Omega$ respectively. Using this data, the materials properties that provide a best fit are: $\sigma = 7.46(10^6)\ (\Omega \cdot m)^{-1}$, $\mu = 3460\ \mu_o$, and $\Theta = 20^\circ$. The magnitude and phase of the experiment and fit are shown in Figures 6 and 7 respectively. For comparison, the predicted response neglecting the effects of eddy currents is also included, and the eddy currents can be seen to have a pronounced effect on the response of the circuit above 100 Hz. The model with eddy currents and hysteresis shows a very good agreement in both magnitude and phase with the test circuit. The agreement with eddy currents but neglecting hysteresis effects is also relatively good, but this model tends to predict more phase lag than was actually observed. The fact that the best fit is achieved by including hysteresis highlights the need for the eventual inclusion of hysteresis effects in the rotating loss model.

5.2 Determination of electrical losses from rundown data

The energy stored in the rotor at any time is

$$E = \frac{1}{2} J \omega^2 \quad (51)$$

The change in energy with respect to time corresponds to power loss, P_{tot} , due to eddy currents, hysteresis, and windage:

$$P_{tot} = -\frac{dE}{dt} = -J \omega \dot{\omega} \quad (52)$$

By measuring the rundown of a shaft in magnetic bearings, the power loss at any speed can be found by substituting the experimental data rundown into (52). However, the loss of interest is not the total loss, but rather the loss component due to magnetic effects. If it is assumed that a linear magnetic model applies, eddy current losses should scale with the square of the bias current level, while windage loss is independent of magnetic effects. By performing rundown tests at several different bias levels, the windage loss and eddy current loss can be separated by a least-squares solution to an over-determined linear algebra problem:

$$\begin{bmatrix} i_{o,1}^2 & 1 \\ i_{o,2}^2 & 1 \\ i_{o,3}^2 & 1 \\ \vdots & \vdots \end{bmatrix} \begin{Bmatrix} P_{eddy} \\ P_{wind} \end{Bmatrix} = \begin{bmatrix} P_{tot,1} \\ P_{tot,2} \\ P_{tot,3} \\ \vdots \end{bmatrix} \quad (53)$$

where $i_{o,k}$ is the bias current level for the k^{th} rundown, P_{eddy} is eddy current loss produced by a 1 Amp bias current, and P_{wind} is windage loss.

This method of identifying rotating loss is less than ideal. Small errors in the measurement of i_o are accentuated by solving (53), and deviations from $P_{eddy} \propto i_o^2$ also cause errors in apparent eddy current power losses. The bearings must also bear the gravitational load of the rotor, resulting in currents that are slightly perturbed from the nominal bias levels. Unfortunately, in the absence of high-speed vacuum chamber rundowns, this method is perhaps the best available to derive rotating eddy current losses from rundown data.

5.3 Comparison of rundown losses to model losses

Losses derived from the model can be compared to the losses derived from rundown tests of the high-speed loss rig of Kasarda *et al.* [8]. This rig consists of a short, thick rotor supported by two radial magnetic bearings. There is no thrust bearing; reluctance centering due to the bias currents in the radial bearings is sufficient to keep the rotor centered axially. The rotor is run up to speed using two induction motors located outboard of either bearing. Once the desired maximum speed is obtained, these motors are retracted from the shaft so as not to influence the rundown losses. The dimensions of this rig necessary for predicting rotating losses are contained in Table 1.

axial length per bearing	4.4 cm
journal inner radius	2.54 cm
journal outer radius	4.55 cm
number of poles	8
number of turns per pole	94
pole width	1.90 cm
lamination thickness	0.3564 mm
lamination conductivity	$7.46(10^6) (\Omega \text{ m})^{-1}$
lamination permeability	$3460 \mu_o$

Table 1: High-speed loss rig dimensions.

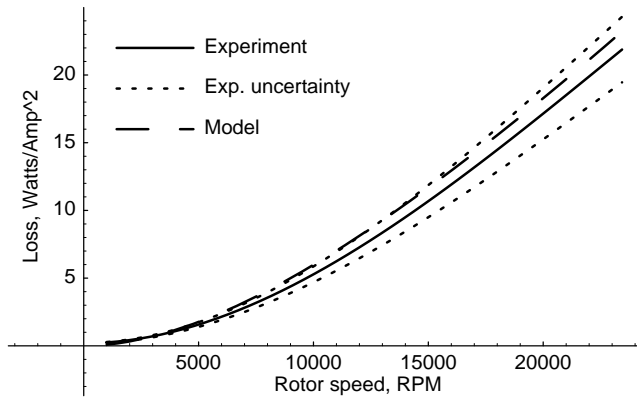


Figure 8: Experimental and predicted rotational losses.

Run-down tests were performed on the rig at three different bias current levels while running the bearing in a NSNS biasing scheme. Using (53), the windage component of the rotating losses was separated from the electrical component, resulting in a profile of eddy current loss per Ampere-squared of bias current versus running speed. This experimental result is compared with losses predicted by a model considering the first 184 harmonics of B in Figure 8. (The error envelope in this figure are due to uncertainty in the measurement of bias current levels for each run-down test. The two boundaries result from calculations based on the nominally specified bias currents and based on the current deduced by the average measured value of flux density in the center of the air gaps. The solid line is the average of these two results). Overall, the predicted losses correspond closely to the measured losses. The model's predictions are within the bounds of experimental uncertainty throughout the entire range of 1000 to 24,000 RPM.

6 Results from the numerical model

Using the model, several long-standing questions with regard to rotating losses in magnetic bearings can be addressed. These questions are:

- Is it better to wind the coils of a bearing in a NSNS or a NNSS configuration?

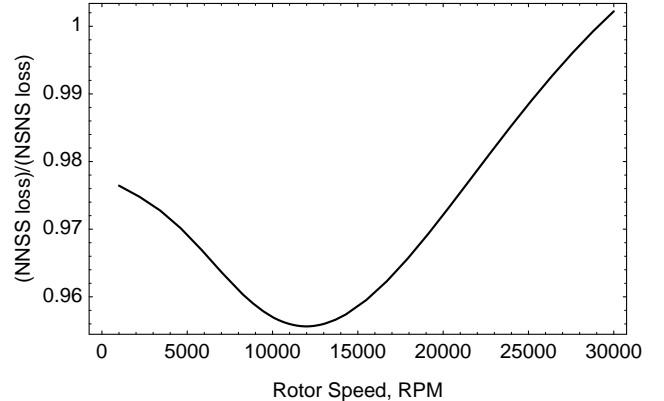


Figure 9: Comparison of NSNS to NNSS losses.

- Do motion-induced eddy currents significantly influence the amount of flux crossing the air gaps, thereby changing the relationship between applied current and resulting force at high speeds?
- At what frequencies do most of the eddy current losses occur?

6.1 NSNS losses versus NNSS losses

Several works have examined the question of whether lower losses result from NSNS or NNSS windings of the bearing's poles [8] [10]. The general conclusion of these works is that lower losses result from NNSS windings than NSNS windings. The present loss model shows a slightly different result. The model of the high-speed loss rig was evaluated using both configurations. A plot of the ratio of the two losses versus rotor speed is shown in Figure 9. This plot shows that NNSS losses are indeed lower at low speeds. However, there is a point at high speed where the losses are equal for both configurations. Beyond this point, NSNS losses are actually lower than NNSS losses for the model of the high-speed loss rig. The explanation for this behavior is that the losses in each configuration arise from different sets of harmonics that change in different ways in response to increasing speed.

6.2 Effect of rotation on flux across the gaps

It has been asserted in [10] that flux across the air gaps is not greatly affected by motion-induced eddy currents in the journal. This claim is supported by the model of the high-speed loss rig. As an example of the variation profile of flux density crossing the surface of the rotor with rotor speed, the model was tested in a NSNS winding configuration at 25 RPM and 25,000 RPM. The average flux distributions about one pole resulting from a one Ampere bias current level are plotted in Figure 10. The dashed line represents the distribution at 25 RPM, and the solid line the distribution at 25,000 RPM. The flux density profile is suppressed at the leading pole edge; however,

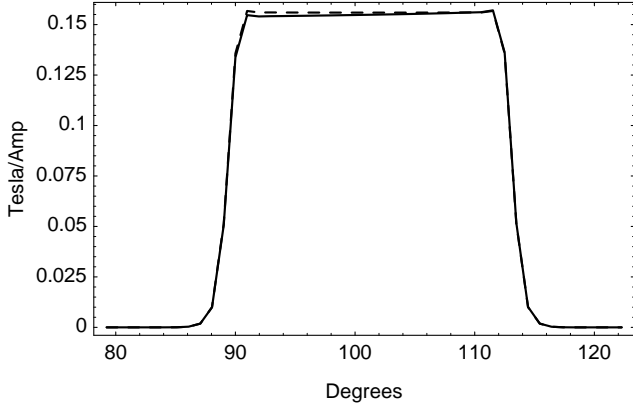


Figure 10: Comparison of flux density profile at 25 and 25,000 RPM.

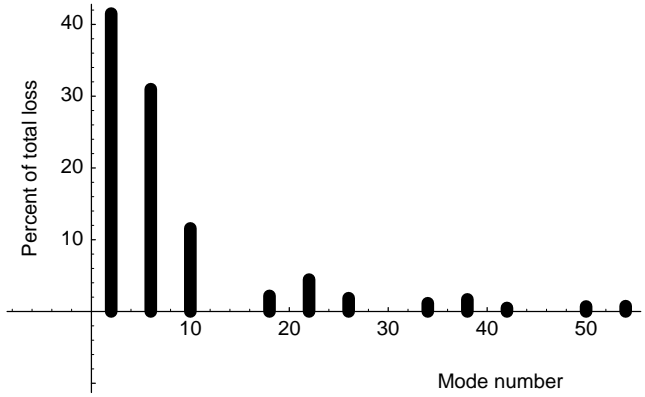


Figure 12: Percent of total loss versus mode number, NNSS case.

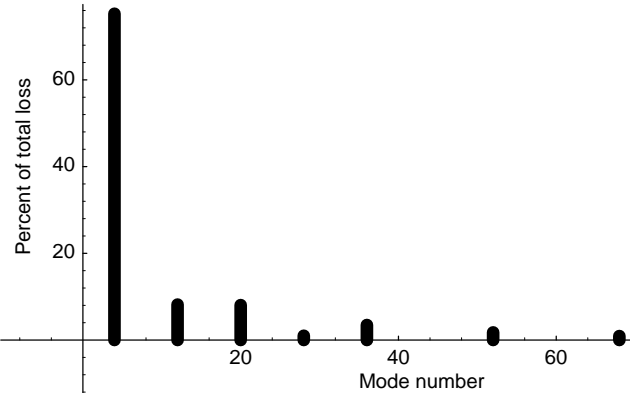


Figure 11: Percent of total loss versus mode number, NSNS case.

the magnitude of the change is very small. There is therefore a negligibly small variation in the relationship between current and force for increasing rotor speed for the model of the high-speed loss rig. However, for bearings with a smaller gap, the change in the flux density profile with speed may be more significant. If the gap is smaller, a higher percentage of the reluctance for any flux path will be carried by the journal iron, accentuating the eddy current effects.

6.3 Distribution of losses

To examine the distribution of losses among various frequency components, the model of the high-speed loss rig was evaluated at 20,000 RPM for both NSNS and NNSS configurations. Losses for the first 184 harmonics were considered in the computational model. Plots of the percentage of total loss attributed to each harmonic are shown for the most significant frequencies in the NSNS case by Figure 11 and for in NNSS case by Figure 12. In the NSNS case, most of the loss is carried in the 4th harmonic. However, significant components also occur in the 12th and 20th harmonics, with about 5% in each. In the NNSS case, however, losses are widely distributed between many harmonics, with the dominant losses oc-

curing in the 2nd, 6th and 10th harmonics. In the NSNS case, most of the losses can be accounted for solely by the 4th mode, providing some justification for using the effective frequency approach for NSNS windings. However, for the NNSS case, losses are widely distributed so that an accurate estimate cannot be obtained by evaluating only at a single frequency. In both cases, however, most of the loss occurs in low harmonic components. This fact implies that minor changes in pole geometry (e.g. rounding the pole tips to “soften” the flux density profile) will only have a small effect on the overall losses.

7 Conclusions

A simplified model of motion-induced eddy currents in the rotating journal of a heteropolar radial magnetic bearing has been considered. Simplifying assumptions used in the analysis are:

- Hysteresis effects are neglected.
- The journal is treated as an “unrolled” periodic sheet.
- Second-order derivatives associated with the plate thickness direction dominate the cross-lamination flux density profile (the thin plate assumption).
- Flux density in the air gaps is two dimensional. The transition to the fully-developed eddy current profile takes place in a negligibly thin region of the journal adjacent to the air-iron interface.

The resulting eddy current model is then solved analytically for the field distribution inside the rotating journal in terms of the magnetic scalar potential applied at the surface of the journal. The analytical solution of the magnetic field inside the rotor is combined with a two-dimensional computational solution of the field in the air between the journal and stator surfaces so that the magnetic field can be computed for arbitrary coil currents. A ring test was used to identify the relevant materials

properties for the rotating loss model. Using the properties found via the ring test, the thin-plate model of rotating losses shows good agreement with experimentally measured power losses from a high-speed magnetically suspended rotor.

Several interesting corollary results arise from the model. First, a NNSS provides lower rotating losses at low speed while a NSNS scheme yields lower losses at very high speeds. Second, most of the losses occur at low number harmonics. Last, the presence of rotationally-induced eddy currents does not significantly affect the profile of average flux density on the surface of the journal. The relationship between applied current and resulting force is nearly constant across a wide range of running speed for bearings with relatively large air gaps.

Several extensions of this work have yet to be considered. The analysis could be expanded to approximately include the effects of hysteresis using a constant phase lag between B and H . The effect of time-varying coil currents is also yet to be included. The present analysis does not address homopolar radial bearings, which are expected to achieve low rotating losses. The thin plate model might be extended to address this configuration, but the analysis would have to be expanded to a three-dimensional domain rather than the pseudo-two-dimensional analysis appropriate for heteropolar bearings.

References

- [1] Stoll, R. L.: *The analysis of eddy currents*. Oxford University Press, 1974.
- [2] J. Avila-Rosales and F. Alvarado, “Nonlinear frequency dependent transformer model of electromagnetic transient studies in power systems,” IEEE Trans. PAS-101(11):4281-4288, Nov. 1982.
- [3] E. J. Tarasiewicz *et al.*, “Frequency dependent eddy current models for nonlinear iron cores,” IEEE Trans. Power Systems, 8(2):588-597, May 1993.
- [4] F. de Leon and A. Semlyen, “Time domain modeling of eddy current effects for transformer transients,” IEEE Trans. Power Delivery, 8(1):271-280, Jan. 1993.
- [5] R. B. Zmood, D. K. Anand, and J. A. Kirk, “The influence of eddy currents on magnetic actuator performance,” *Proceedings of the IEEE* 75(2):259-60, 1987.
- [6] D. C. Meeker, E. H. Maslen, and M. D. Noh, “An augmented magnetic circuit model for magnetic bearings including eddy currents, fringing, and leakage,” *IEEE Transactions on Magnetics*, to appear.
- [7] C. Guerin *et al.*, “A shell element for computing 3D eddy currents – application to transformers,” *IEEE Transactions on Magnetics*, 31(3):1360-1363, May 1995.
- [8] M. E. F. Kasarda *et al.*, “Design of a high speed rotating loss test rig for radial magnetic bearings,” *Proceedings of the Fourth International Symposium on Magnetic Bearings*, Zurich, 1994.
- [9] L. S. Stephens, *Design and control of active magnetic bearings for a high speed machining spindle*, doctoral dissertation, University of Virginia, 1995.
- [10] F. Matsumura and K. Hatake, “Relation between magnetic pole arrangement and magnetic loss in magnetic bearing,” *Proceedings of the Third International Symposium on Magnetic Bearings*, Alexandria, VA, July 1992.
- [11] S. R. Hoole, *Computer-aided analysis and design of electromagnetic devices*, New York: Elsevier, 1989.
- [12] C. A. Brebbia and J. Dominguez, *Boundary elements: an introductory course*, New York: McGraw-Hill, 1989.